Astronomy & Astrophysics

The orbits of subdwarf-B + main-sequence binaries

II. Three eccentric systems; BD +29°3070, BD +34°1543 and Feige 87[⋆]

J. Vos[1], R. H. Østensen[1], P. Németh[1], E. M. Green[2], U. Heber[3], and H. Van Winckel[1]

[1] Instituut voor Sterrenkunde, KU Leuven, Celestijnenlaan 200D, 3001 Leuven, Belgium
 e-mail: jorisv@ster.kuleuven.be
[2] Steward Observatory, University of Arizona, 933 North Cherry Avenue, Tucson, AZ 85721, USA
[3] Dr. Remeis-Sternwarte Astronomisches Institut, Universität Erlangen-Nürnberg, 96049 Bamberg, Germany

ABSTRACT

Context. The predicted orbital-period distribution of the subdwarf-B (sdB) population is bi-modal with a peak at short (<10 days) and long (>250 days) periods. Observationally, many short-period sdB systems are known, but the predicted long period peak is missing as orbits have only been determined for a few long-period systems. As these predictions are based on poorly understood binary-interaction processes, it is of prime importance to confront the predictions with reliable observational data. We therefore initiated a monitoring program to find and characterize long-period sdB stars.
Aims. In this paper we aim to determine the orbital parameters of the three long-period sdB+MS binaries BD+29°3070, BD+34°1543 and Feige 87, to constrain their absolute dimensions and the physical parameters of the components.
Methods. High-resolution spectroscopic time series were obtained with HERMES at the *Mercator* telescope on La Palma, and analyzed to determine the radial velocities of both the sdB and MS components. Photometry from the literature was used to construct the spectral-energy distribution (SED) of the binaries. Atmosphere models were used to fit these SEDs and to determine the surface gravities and temperatures of both components of all systems. Spectral analysis was used to check the results of the SEDs.
Results. An orbital period of 1283 ± 63 d, a mass ratio of $q = 0.39 \pm 0.04$ and a significant non-zero eccentricity of $e = 0.15 \pm 0.01$ were found for BD+29°3070. For BD+34°1543 we determined $P_{\rm orb} = 972 \pm 2$ d, $q = 0.57 \pm 0.01$ and again a clear non-zero eccentricity of $e = 0.16 \pm 0.01$. Last, for Feige 87 we found $P_{\rm orb} = 936 \pm 2$ d, $q = 0.55 \pm 0.01$ and $e = 0.11 \pm 0.01$.
Conclusions. BD+29°3070, BD+34°1543 and Feige 87 are long period sdB + MS binaries on clearly eccentric orbits. These results are in conflict with the predictions of stable Roche-lobe overflow models.

Key words. binaries: spectroscopic – stars: evolution – stars: fundamental parameters – subdwarfs

1. Introduction

Hot subdwarf-B (sdB) stars are core helium burning stars with a very thin hydrogen envelope ($M_{\rm H} < 0.02\ M_\odot$), and a mass close to the core helium flash mass ~0.47 $M_\odot$ (Saffer et al. 1994; Brassard et al. 2001). These hot subdwarfs are found in all galactic populations, and they are the main source for the UV-upturn in early-type galaxies (Green et al. 1986; Greggio & Renzini 1990; Brown et al. 1997). Furthermore, their photospheric chemical composition is governed by diffusion processes causing strong He-depletion and other chemical peculiarities (Heber 1998). The formation of these extreme horizontal branch objects is still puzzling. To form an sdB star, its progenitor needs to lose its hydrogen envelope almost completely before reaching the tip of the red giant branch (RGB), so that the core ignites while the remaining hydrogen envelope is not massive enough to sustain hydrogen shell burning. A variety of possible formation channels have been proposed. The earlier suggestions were based on single star evolution, e.g. stellar wind mass loss near the tip of the RGB (D'Cruz et al. 1996) or enhanced mass loss due to rotationally driven helium mixing (Sweigart 1997). It was found, however, that many sdB stars reside in binary systems (Maxted et al. 2001), indicating that binary interaction plays an important role (Mengel et al. 1976). Currently, there is a consensus that sdB stars are formed by binary evolution only,

and several evolutionary channels have been proposed, where binary-interaction physics plays a major role. Close binary systems can be formed in a common envelope (CE) ejection channel (Paczynski 1976), while stable Roche-lobe overflow (RLOF) can produce wide sdB binaries (Han et al. 2000, 2002). An alternative formation channel forming a single sdB star is the double white dwarf (WD) merger, where a pair of white dwarfs spiral in to form a single sdB star (Webbink 1984).

Han et al. (2002, 2003) addressed these three binary formation mechanisms, and performed binary population synthesis (BPS) studies for two kinds of CE ejection channels, two possible stable RLOF channels and the WD merger channel. The CE ejection channels produce close binaries with periods of $P_{\rm orb} = 0.1-10$ d, and main-sequence (MS) or WD companions. The sdB binaries formed through stable RLOF have orbital periods ranging from 10 to 500 days, and MS companions. An alternative stable RLOF channel based on the γ-formalism is described by Nelemans et al. (2000, 2001); Nelemans (2010) can produce sdB binaries with periods on the order of 1−2 years. Finally, The WD merger channel can lead to sdB stars with a higher mass, up to 0.65 $M_\odot$. A detailed review of hot subdwarf stars is given by Heber (2009).

Many observational studies have focused on short-period sdB binaries (Koen et al. 1998; Maxted et al. 2000, 2001; Heber et al. 2002; Morales-Rueda et al. 2003; Napiwotzki et al. 2004; Copperwheat et al. 2011), and over 100 of these systems are currently known (Geier et al. 2011, Appendix A). These

---

[⋆] Tables 1–4 and 6 are available in electronic form at
http://www.aanda.org

observed short-period sdB binaries correspond very well with the results of BPS studies. However, only a few long period sdB binaries are known (Green et al. 2001; Østensen & Van Winckel 2011, 2012; Deca et al. 2012; Barlow et al. 2012; Vos et al. 2012), and the current studies show that there are still large discrepancies between theory and observations (Geier 2013). In a recent response to these discoveries Chen et al. (2013) have revisited the RLOF models of Han et al. (2003) with more sophisticated treatment of angular momentum loss. Their revised models show mass – orbital period relations that increase substantially as a function of composition, with solar metallicity models reaching periods up to 1100 d. They also note that by allowing the transfer of material extending beyond the classic Roche lobe (atmospheric RLOF) they can reach periods as long as ~1600 d.

In this paper we present the orbital and atmospheric parameters of the three long-period sdB + MS binaries BD+29°3070, BD+34°1543 and Feige 87, using the methods described in Vos et al. (2012), hereafter Paper I. In Sect. 2 the radial velocities are determined for both components after which the orbital parameters are derived. Using the obtained mass ratio, the atmospheric parameters are derived from the spectral-energy distribution (Sect. 3), and spectral analysis (Sect. 4). Furthermore, the surface gravity of the sdB component is estimated based on the gravitational redshift in Sect. 5. Finally in Sects. 6 and 8 all results are summarized. BD+29°3070, BD+34°1543 and Feige 87 are part of a long-term spectroscopic monitoring program, and preliminary results of these and five more systems in this program were presented in Østensen & Van Winckel (2011, 2012).

2. Spectroscopy

High resolution spectroscopic observations of BD+29°3070, BD+34°1543 and Feige 87 were obtained with the HERMES spectrograph (High Efficiency and Resolution *Mercator* Echelle Spectrograph, $R = 85\,000$, 55 orders, 3770−9000 Å, Raskin et al. 2011) attached to the 1.2-m *Mercator* telescope at the Roque de los Muchachos Observatory, La Palma. HERMES is connected to the *Mercator* telescope by an optical fiber, and is located in a temperature controlled enclosure to ensure optimal wavelength stability. In Paper I, Sect. 2 the wavelength stability was checked, using 38 radial velocity standard stars of the IAU observed over a time span of 1481 days, and a standard deviation of 80 m s^{-1} with a non-significant shift to the IAU radial velocity standard scale was found. In total there were 31 spectra of BD+29°3070, 30 of BD+34°1543 and 33 of Feige 87 taken between June 2009 and January 2013. The observations are summarized in Table 1. HERMES was used in high-resolution mode, and Th-Ar-Ne exposures were made at the beginning and end of the night. The exposure time of the science observations was adapted to reach a signal-to-noise ratio (S/N) of 25 in the *V*-band, whenever observing conditions permitted. The HERMES pipeline v5.0 was used for the basic reduction of the spectra, including barycentric correction.

For BD+34°1543 there was one more high resolution spectrum available, taken with the FOCES spectrograph (Fiber-Optics Cassegrain Echelle Spectograph, $R = 30\,000$, 3600−6900 Å) attached to the 2.2-m telescope at Calar Alto observatory, Spain. This spectrum was obtained in February 2000 (HJD = 2 451 576.5166). The spectrum was reduced as described in Pfeiffer et al. (1998) using the IDL macros developed by the Munich Group.

Flux-calibrated spectra of BD+29°3070, BD+34°1543, and Feige 87 were taken with the Boller and Chivens (B&C)

spectrograph attached to the University of Arizona's 2.3 m Bok telescope located on Kitt Peak. All three stars were observed using a 2.5″ slit and 1st order 400/mm grating blazed at 4889 A, with a UV-36 filter to block 2nd order light. These parameters provided a 9 Å resolution over the wavelength range 3600−6900 Å. BD+29°3070 was observed on 25-06-2000 with an exposure time of 30 s, resulting in an overall S/N of 235 per resolution element (134 per pixel, and slightly higher in the range 3600−5000 Å). BD+34°1543 was observed once on 17-09-1998 and five additional times between 2005 and 2007, for a total exposure time of 260 s and a (formal) $S/N \sim 750$ (435 per pixel). Feige 87 was observed twice, on 10-03-1999 and 06-06-1999, for a total exposure time of 210 s and S/N of 345 (195 per pixel). The spectra were bias-subtracted, flat-fielded, optimally extracted, and wavelength calibrated using standard IRAF[1] tasks. They were flux calibrated using either BD+28°4211 or Feige 34 as flux standards. The individual spectra for BD+34°1543 and Feige 87 were combined by determining the cross-correlation velocities using only the Balmer and helium lines, and shifting each spectrum to the mean sdB velocity before combining (although the velocity shifts were always small, less than 1/3 of a pixel, compared to the spectral resolution 3.15 pixels). While these spectra have a too low resolution to obtain radial velocities, they are used to determine spectroscopic parameters of both components in Sect. 4.3.

2.1. Radial velocities

Østensen & Van Winckel (2011) determined preliminary orbital periods of both BD+29°3070, BD+34°1543 and Feige 87 based on the radial velocities of the cool companion and assuming circular orbits, resulting in respectively 1160 ± 67 days, 818 ± 21 days and 915 ± 16 days. These long periods allow us to sum spectra that are taken within a five-day interval to increase the S/N, without significantly smearing or broadening the spectral lines. This five-day interval corresponds to about 0.5% of the orbital period, and a maximum radial velocity shift of 0.06 km s^{-1}. After this merging, 28 spectra of BD+29°3070, 22 spectra of BD+34°1543 and 19 spectra of Feige 87 remain, with a S/N varying from 25 to 50. These spectra with the averaged BJD in case of the merged spectra are displayed in Tables 2–4.

The radial velocities of the MS components are determined with the cross-correlation method of the HERMES pipeline, based on a discrete number of line positions. This is possible because the sdB component has only a few H and He lines, which are avoided in the cross correlation. To determine the radial velocities of the MS components of the three systems, a G2-type mask was used on orders 55−74 (4780−6530 Å) as these orders give the best compromise between maximum S/N for G-K type stars and absence of telluric influence. The final errors on the radial velocities (see Tables 2–4) are calculated taking into account the formal errors on the Gaussian fit to the normalized cross-correlation function and the error due to the stability of the wavelength calibration.

To determine the radial velocities of the sdB components a different technique is necessary as these stars have only few spectral lines visible in the composite spectra. The only spectral line that is not contaminated by the MS components is the He I blend at 5875.61 Å. To derive the radial velocity based

---

[1] IRAF is distributed by the National Optical Astronomy Observatory; see http://iraf.noao.edu/

Table 5. Spectroscopic orbital solutions for both the main-sequence (MS) and subdwarf-B (sdB) component of BD+29°3070, BD+34°1543, and Feige 87.

Parameter	BD+29°3070 MS	BD+29°3070 sdB	BD+34°1543 MS	BD+34°1543 sdB	Feige 87 MS	Feige 87 sdB
P (d)	1283 ± 63		972 ± 2		936 ± 2	
T_0	2 453 877 ± 41		2 451 519 ± 11		2 453 259 ± 21	
e	0.15 ± 0.01		0.16 ± 0.01		0.11 ± 0.01	
ω	1.60 ± 0.22		1.58 ± 0.07		2.92 ± 0.15	
q	0.39 ± 0.01		0.57 ± 0.01		0.55 ± 0.01	
γ (km s^{-1})	−57.58 ± 0.36	−56.8 ± 0.9	32.10 ± 0.06	33.12 ± 0.15	32.98 ± 0.08	34.32 ± 0.16
K (km s^{-1})	6.53 ± 0.31	16.6 ± 0.6	5.91 ± 0.07	10.31 ± 0.22	8.19 ± 0.11	15.01 ± 0.21
$a \sin i$ ($R_\odot$)	164 ± 15	416 ± 35	112 ± 2	196 ± 4	150 ± 2	276 ± 3
$M \sin^3 i$ ($M_\odot$)	1.15 ± 0.19	0.45 ± 0.08	0.27 ± 0.01	0.15 ± 0.01	0.77 ± 0.03	0.42 ± 0.01

Notes. a denotes the semi-major-axis of the orbit. The quoted errors are the standard deviation from the results of 5000 iterations in a Monte-Carlo simulation.

on only one line, a more specific method is necessary to avoid unacceptably high errors. The region around the He I line is first cleaned by hand of all remaining cosmic rays after which it is normalized by fitting low order polynomials to the spectrum. The cleaned and normalized spectra are then cross correlated with a high-resolution synthetic sdB spectrum from the LTE grids of Heber et al. (2000). For all three systems a synthetic spectrum of $T_{\rm eff}$ = 30 000 K, log g = 5.50 dex, and a resolution matching that of HERMES was used. Spectra with different $T_{\rm eff}$ and log g were tried, but did not result in a significant change. The cross correlation (CC) is carried out in wavelength space, and the resulting radial velocity is calculated by fitting a Gaussian to the cross-correlation function. The error is determined by performing a Monte-Carlo (MC) simulation in which Gaussian noise is added to the observed spectra after which the CC is repeated. The final error is based on the standard deviation of the radial-velocity results of 1000 MC iterations, the wavelength stability of HERMES and the dependence on the used sdB template. For a more elaborate explanation on the derivation of radial velocities from the HERMES spectra see Paper I, Sect. 2.1. The final radial velocities of both the MS and sdB component of BD+29°3070 together with their errors are given in Table 2, while those of BD+34°1543 and Feige 87 can be found in Table 3 and 4 respectively.

The FOCES spectrum of BD+34°1543 is analyzed in exactly the same way as the HERMES spectra to determine the radial velocities of both components. The results are given in Table 3 together with the HERMES results.

2.2. Orbital parameters

The orbital parameters of the sdB and MS components are calculated by fitting a Keplerian orbit to the radial velocity measurements, while adjusting the period (P), time of periastron (T_0), eccentricity (e), angle of periastron (ω), two amplitudes ($K_{\rm MS}$ and $K_{\rm sdB}$) and two systemic velocities ($\gamma_{\rm MS}$ and $\gamma_{\rm sdB}$). As a first guess for these parameters, the results of Østensen & Van Winckel (2011) were used. The radial velocity measurements were weighted according to their errors as $w = 1/\sigma$. For each system, the Lucy & Sweeney (1971) test was used to check if the orbit is significantly eccentric. In the fitting process, the system velocities of both components are allowed to vary independently of each other, to allow for gravitational redshift effects in the sdB component (see Paper I, Sects. 4, and 5 in this paper). The uncertainties on the final parameters are obtained using 5000 iterations in a Monte-Carlo simulation where

the radial velocities were perturbed based on their errors. The spectroscopic parameters of BD+29°3070 and BD+34°1543 are shown in Table 5. The radial-velocity curves and the best fits are plotted in Fig. 1.

Feige 87 (=PG 1338+611) has been studied by Barlow et al. (2012) as part of a long term observing program with the Hobby-Eberly telescope lasting from January 2005 till March 2008. They published radial velocities for both the MS and sdB component. However, Barlow et al. (2012) find a difference in systemic velocity for the MS and sdB component of $\gamma_{\rm sdB} - \gamma_{\rm MS} = -2.1 \pm 1.0$ km s^{-1} (compared to $\gamma_{\rm sdB} - \gamma_{\rm MS} = 1.30 \pm 0.11$ km s^{-1} for the HERMES spectra), which they attribute to gravitational redshift. If this was caused by gravitational redshift, this shift would mean that the MS component has a higher surface gravity than the sdB component, a highly unlikely situation (see also Sect. 5). A more plausible cause can be found in the lines used to derive the radial velocities of the sdB component. Barlow et al. (2012) used both the He I λ 4472 and He I λ 5876 lines, but when comparing the He I λ 4472 line with a synthetic G2 spectrum, it is clear that this line is significantly contaminated by spectral features of the cool companion. In the analysis of the radial-velocity curves of Feige 87, we used their results of Barlow et al. (2012) of the MS component, but discarded the results of the sdB component. The phase-folded radial velocity curve of the HERMES data is shown in Fig. 1, while the radial velocity curve of both HERMES and Barlow et al. (2012) is shown in Fig. 2. The spectroscopic parameters of Feige 87 are given in Table 5.

3. Spectral energy distribution

The spectral-energy distribution (SED) of the systems can be used to determine the spectral type of the MS and sdB component. We used photometric SEDs which were fitted with model SEDs to determine both the effective temperature and surface gravity of both components.

3.1. Photometry

To collect the photometry of both systems the subdwarf database[2] (Østensen 2006), which contains a compilation of data on hot subdwarf stars collected from the literature, is used. These photometric measurements are supplemented with photometry obtained from several other catalogs as listed in Table 6. In total we obtained 17 photometric measurements for BD+29°3070,

---

[2] http://catserver.ing.iac.es/sddb/
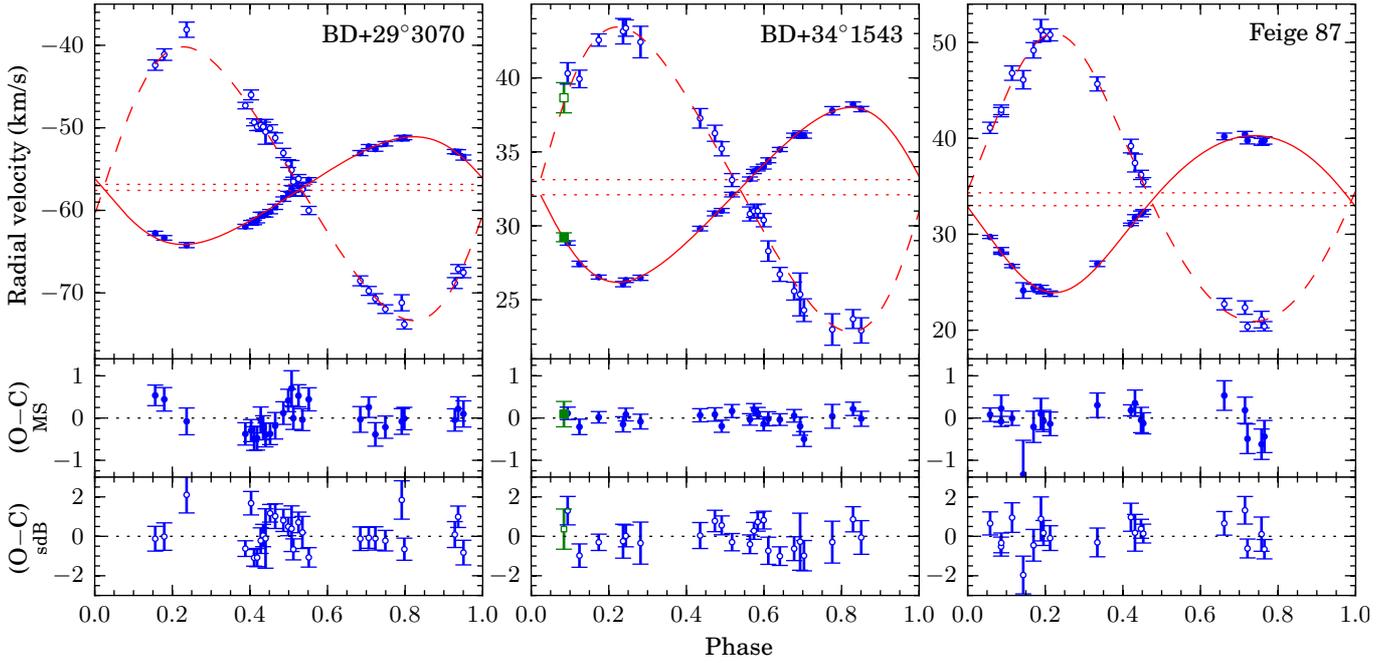
Fig. 1. Radial velocity curves for BD+29°3070 (*left*), BD+34°1543 (*center*) and Feige 87 (*right*). *Top*: spectroscopic orbital solution (solid line: MS, dashed line: sdB), and the observed radial velocities (HERMES: blue circles, FOCES: green squares, filled symbols: MS component, open symbols: sdB component). The measured system velocities of both components are shown by a dotted line. *Middle*: residuals of the MS component. *Bottom*: residuals of the sdB component.
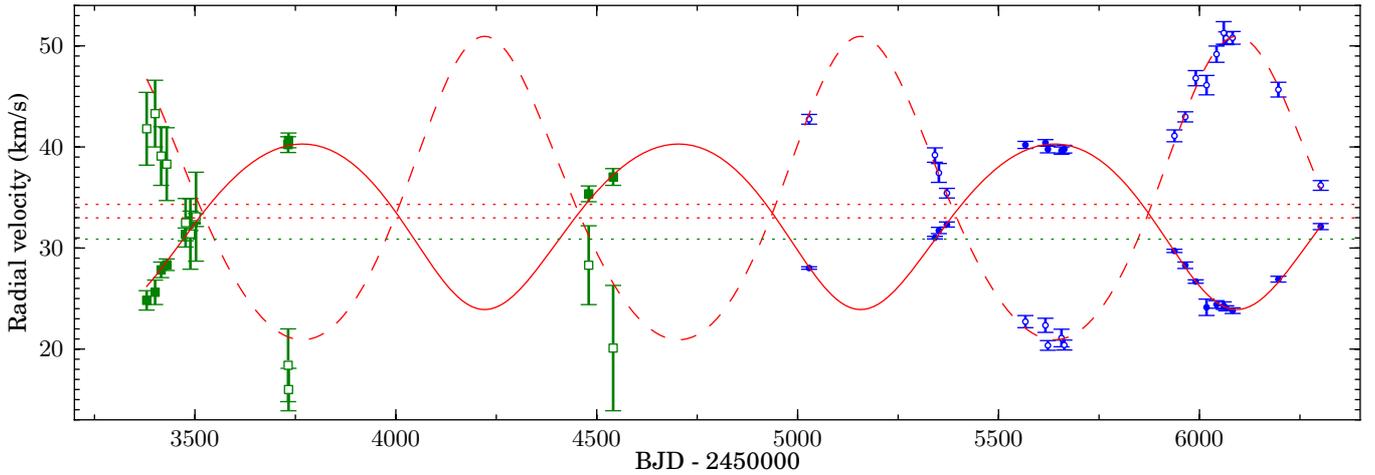
Fig. 2. Radial velocity curve of Feige 87, showing the spectroscopic orbital solution (solid line: MS, dashed line: sdB), and the observed radial velocities (HERMES: blue circles, Barlow et al.: green squares, filled symbols: MS component, open symbols: sdB component). The measured system velocities of both components based on the HERMES data and the MS radial velocities of Barlow et al. are shown by a dotted red line, while the system velocity of the sdB component based on the data of Barlow et al. is plotted in a green dotted line.

14 for BD+34°1543 and 11 for Feige 87. Both accurate photometric measurements at short and long wavelengths are used to establish the contribution of the hot sdB component and the cool MS component.

3.2. SED fitting

The SED fitting method is similar to the one described in Paper I. The observed photometry is fitted with a synthetic SED integrated from model atmospheres. For the MS component Kurucz atmosphere models (Kurucz 1979) ranging in effective temperature from 4000 to 9000 K, and in surface gravity from $\log g = 3.0$ dex (cgs) to 5.0 dex (cgs) are used. For the hot

sdB component TMAP (Tübingen NLTE Model-Atmosphere Package, Werner et al. 2003) atmosphere models with a temperature range from 20 000 K to 50 000 K, and $\log g$ from 4.5 dex (cgs) to 6.5 dex (cgs) are used.

The SEDs are fitted in two steps. First the grid based approach described in Degroote et al. (2011) extended for binarity is used to scan the entire parameter space. For each point the χ^2 is calculated as

$$\chi^2 = \sum_i \frac{(O_i - C_i)^2}{\xi_i^2}, \tag{1}$$

where O_i is the observed photometry and C_i is the calculated model photometry. The grid point with the lowest χ^2 is used as

starting point for a least-squares minimizer which will then determine the final result. In a binary system, there are eight parameters to consider: the effective temperatures ($T_{eff,MS}$ and $T_{eff,sdB}$), surface gravities (g_{MS} and g_{sdB}) and radii (R_{MS} and R_{sdB}) of both components, the interstellar reddening $E(B - V)$ and the distance (d) to the system. The interstellar reddening is presumed equal for both the MS and the sdB component. To increase the accuracy, the models are first corrected for interstellar reddening and then integrated over the photometric pass-bands using the reddening law of Fitzpatrick (2004) with $R_V = 3.1$. The distance to the system is used as a scale factor and is calculated analytically, by shifting the synthetic models to the photometric observations.

As shown in Paper I, the mass ratio obtained from the radial velocity curves can be used to couple the radii of both components to their surface gravity, and thus reducing the number of free parameters from eight to six. The total flux of a binary system is then calculated using:

$$F_{tot}(\lambda) = \frac{G M_{MS}}{d^2 g_{MS}} \left(F_{MS}(\lambda) + q \frac{g_{MS}}{g_{sdB}} F_{sdB}(\lambda) \right). \quad (2)$$

The uncertainties on the final parameters are determined by calculating two-dimensional confidence intervals (CI) for all parameter pairs. This is done by creating a 2D-grid for each parameter pair. For each point in this grid, the two parameters for which the CI is calculated are kept fixed on the grid-point value, while the least-squares minimizer is used to find the best-fitting values for all other parameters. The resulting χ^2 for each point in this grid is stored. All these χ^2s are then rescaled so that the χ^2 of the best fit has the expected value $k = N_{obs} - N_{free}$, with N_{obs} the number of observations and N_{free} the number of free parameters in the fit. The cumulative density function (CDF) is used to calculate the probability of a model to obtain a certain χ^2 value as:

$$F(\chi^2, k) = P\left(\frac{k}{2}, \frac{\chi^2}{2} \right). \quad (3)$$

Where P is the regularized Γ-function. Based on the obtained probability distribution, the uncertainties on the parameters can be derived.

3.3. Results

To fit the SEDs of the three systems, first a grid of composite binary spectra is calculated for 1 000 000 points randomly distributed over the T_{eff}, $\log g$ and $E(B - V)$ intervals for both components. Then the 50 best-fitting grid points are used as starting values for the least-squares minimizer. For this best fit the CIs are estimated, and used to limit the original ranges on the parameters, after which the fitting process (grid search and least-squares minimizer) is repeated. To determine the CIs of the parameters, for each two parameters a grid with a resolution of 45×45 points was used, with the limits adjusted based on the resulting confidence intervals. When the model atmospheres allowed, the limits of the grid are set to include the 95% CI, when this was not possible, the limits of the model atmosphere grid were used. The final uncertainties on the parameters are an average of the 95% CIs for that parameter in all two-dimensional CIs that contain that parameter.

The photometry of BD+29°3070 has a rather large spread, which will result in large uncertainties on the derived parameters. The best fitting effective temperatures are $T_{eff,MS} = 6570 \pm 550$ K and $T_{eff,sdB} = 28\,500 \pm 5000$ K, with surface gravities of $\log g_{MS} = 4.4 \pm 0.5$ dex and $\log g_{sdB} = 5.76 \pm 0.5$ dex. The

reddening is $E(B - V) = 0.009^{+0.041}_{-0.009}$ mag. This value is consistent with the maximum reddening $E(B - V)_{max} = 0.052$ derived from the dust maps of Schlegel et al. (1998). The χ^2 of the best fit is 45.6 which is more than three times as high as the expected value ($N_{obs} - N_{free} = 12$), indicating that the stated errors on the photometry are too small. When calculating the confidence intervals, a scaling factor of 3.8 is used when converting the χ^2 values to probabilities. As can be seen on the plots of the CIs in Fig. 4, there is no strong constraint possible on the surface gravity of the components. Increasing the surface gravity of one component can be countered by increasing the $\log g$ of the other component as well, and thus effectively shrinking the radii of both components. For the sdB component there is a strong correlation between T_{eff} and $\log g$ visible. The effect on the atmosphere models of an increase in T_{eff} can be diminished by increasing $\log g$, and thus decreasing the radius. However, it is possible to provide an upper limit on the effective temperature as the He II lines are not visible in the HERMES spectra, indicating that the effective temperature is below 35 000 K (Heber 2009).

For BD+34°1543 fourteen photometric measurements are available, with a smaller spread than for BD+29°3070. The effective temperatures of the components derived from the SED fit are $T_{eff,MS} = 6210 \pm 250$ K and $T_{eff,sdB} = 36\,700 \pm 5000$ K, while a surface gravity of $\log g_{MS} = 4.19 \pm 0.20$ dex and $\log g_{sdB} = 5.92 \pm 0.40$ dex are found. The reddening is determined to be $E(B - V) = 0.007^{+0.061}_{-0.007}$ which is consistent with the maximum reddening found on the dust maps of Schlegel et al. (1998), and supported by the absence of sharp interstellar absorption lines in the spectrum. As can be seen in Fig. 4 the probability distributions of the MS components parameters form a Gaussian-like pattern, and the T_{eff} and $\log g$ of the MS component have stronger constraints than for BD+29°3070, independently of the parameters for the sdB components. The uncertainty on the effective temperature and surface gravity of the sdB component is larger as both parameters are correlated in the same way as for BD+29°3070. However, the presence of clearly visible He I and He II lines in the HERMES spectra of BD+34°1543 indicates that the effective temperature should be between 35 000 and 50 000 K.

In the case of BD+34°1543 the parallax was measured by HIPPARCOS (van Leeuwen 2007) to be 4.22 ± 1.72 mas. This parallax could be used to fix the distance to the system in the SED fitting process. Since the parallax is of the same order as the projected size of the orbit for this system, one may presume that the HIPPARCOS parallax is unreliable, but as both components of BD+34°1543 have a very similar flux in the HIPPARCOS pass band, the center of light does not change during the orbit. However, the uncertainty on the parallax is large (~40%). Using this parallax to fix the distance to the system, without propagating the uncertainty on it, results in effective temperatures of $T_{eff,MS} = 6230 \pm 100$ K and $T_{eff,sdB} = 37\,900 \pm 3500$ K, and surface gravities of $\log g_{MS} = 4.04 \pm 0.05$ dex and $\log g_{sdB} = 5.81 \pm 0.15$ dex. The reddening is determined to be $E(B - V) = 0.011^{+0.057}_{-0.011}$. The uncertainties are much smaller as when the distance is included as a free parameter, especially on the surface gravity. However, due to the large uncertainty on the parallax, only the atmospheric parameters derived with the distance as a free parameter are used.

For Feige 87 there are only eleven photometric measurements found in the literature, but there is a very good agreement between all the measurements in the different bands. When checking the residuals of the fit, Feige 87 has the smallest spread of all three systems, with a total χ^2 of 2.9. The SED results
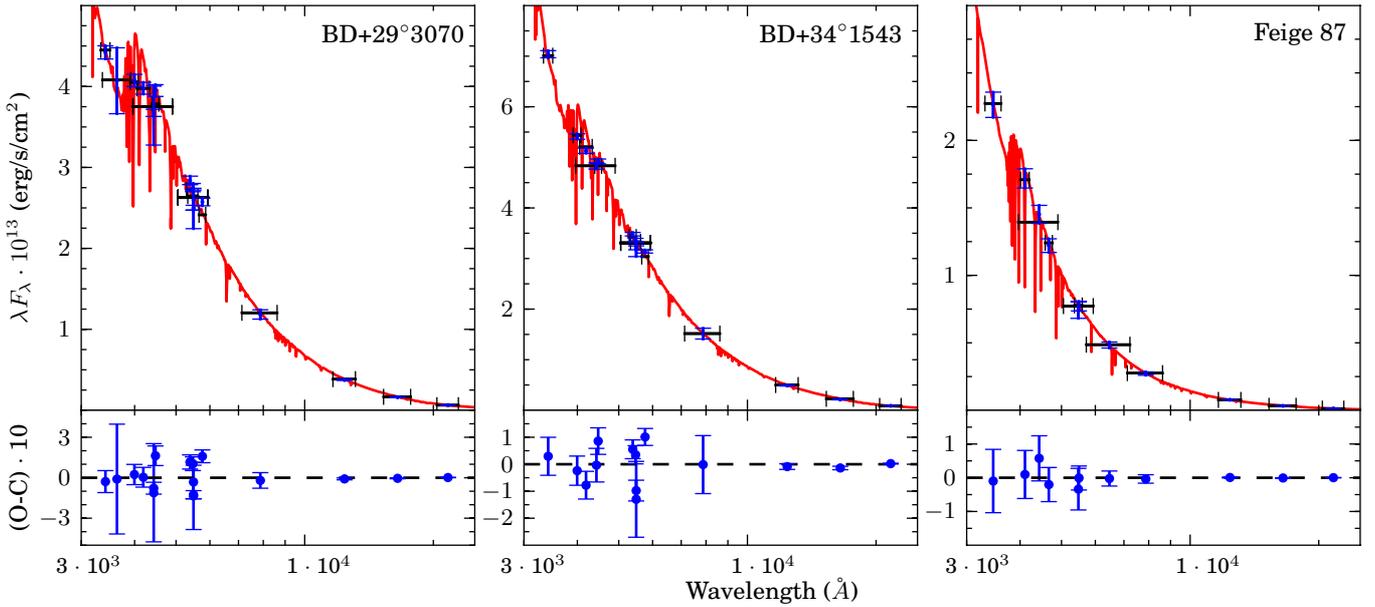
Fig. 3. Spectral energy distribution and (O−C) of BD+29°3070 (*left*), BD+34°1543 (*center*) and Feige 87 (*right*). The measurements are given in blue, the integrated synthetic models are shown in black, where a horizontal error bar indicates the width of the pass-band. The best fitting model is plotted in red. In the *bottom panels* the residuals are plotted for each system.

Table 7. Results of the SED fit for BD+29°3070, BD+34°1543 and Feige 87, together with the 95% probability intervals derived from the confidence intervals plotted in Fig. 4.

Parameter	BD+29°3070		BD+34°1543		Feige 87	
	Best fit	95%	Best fit	95%	Best fit	95%
$T_{\mathrm{eff,MS}}$ (K)	6570	5800–7100	6210	6000–6440	5840	5300–6400
$\log g_{\mathrm{MS}}$ (dex)	4.40	4.00–4.80	4.19	4.05–4.35	4.40	4.15–4.60
$T_{\mathrm{eff,sdB}}$ (K)	28 500	24 000–36 000	36 700	30 000–/	27 400	21 000–33 000
$\log g_{\mathrm{sdB}}$ (dex)	5.76	5.20–6.20	5.92	5.75–6.05	5.54	5.20–5.80
$E(B - V)$	0.007	0–0.052	0.007	0–0.068	0.012	0–0.057

Notes. For some parameters the confidence intervals could not be calculated due to the limited range of the model atmospheres.

in an effective temperature of $T_{\mathrm{eff,MS}}$ = 5840 ± 500 K and $T_{\mathrm{eff,sdB}}$ = 27 400 ± 5000 K for the MS and sdB component, together with a surface gravity of $\log g_{\mathrm{MS}}$ = 4.40 ± 0.30 dex and $\log g_{\mathrm{sdB}}$ = 5.50 ± 0.50 dex. The reddening of the system is found to be $E(B - V) = 0.012^{+0.045}_{-0.012}$, consistent with the results from the dust maps of Schlegel et al. (1998). On Fig. 4 the probability distributions show a similar pattern as for BD+29°3070. Although the distribution in $T_{\mathrm{eff,MS}} - \log g_{\mathrm{MS}}$ and $T_{\mathrm{eff,sdB}} - T_{\mathrm{eff,MS}}$ have a clearer Gaussian pattern, indicating that they are determined more accurate as for BD+29°3070.

The advantage of having an estimate of the distance to the target is clear when considering the uncertainties of the atmospheric parameters. Because the radii of the components are derived from their surface gravity, limiting the distance will also limit the radii. If the distance is accurately known, the accuracy of the surface gravity can be increased by a factor ten compared to when the distance is treated as a free parameter. Determining atmospheric parameters from photometry will greatly benefit from the Gaia mission that will derive accurate distances of about a billion stars.

4. Spectral analysis

The atmospheric parameters determined from the SEDs can be checked using the spectra. The HERMES echelle spectra are not

easy to flux calibrate accurately, and therefore not well suited to fit model atmospheres, but it is possible to subtract the continuum contribution of the sdB component as explained in the following subsection. The resulting spectra of the MS components can be used to derive atmospheric parameters based on the Fe I and Fe II lines. Apart from the HERMES spectra, we have obtained flux calibrated long-slit spectra with the Bok telescope (see Sect. 4.3). The resolution of these spectra is too low to determine radial velocities, but they can be used to fit model atmospheres and provide an independent set of atmospheric parameters.

4.1. Disentangling

When the spectroscopic parameters of both components in a system are known, it is possible to extract the spectrum of the MS component from the combined spectrum. This is done by subtracting a synthetic sdB spectrum with a surface gravity and effective temperature determined from the SED fit. As the sdB component only has a few lines and only wavelength regions that don't contain balmer or He lines are used, this is equivalent to subtracting the continuum contribution of the sdB component.

Each HERMES spectrum is treated separately. First the HERMES response curve is removed from the spectrum after which its continuum is determined by fitting a low degree
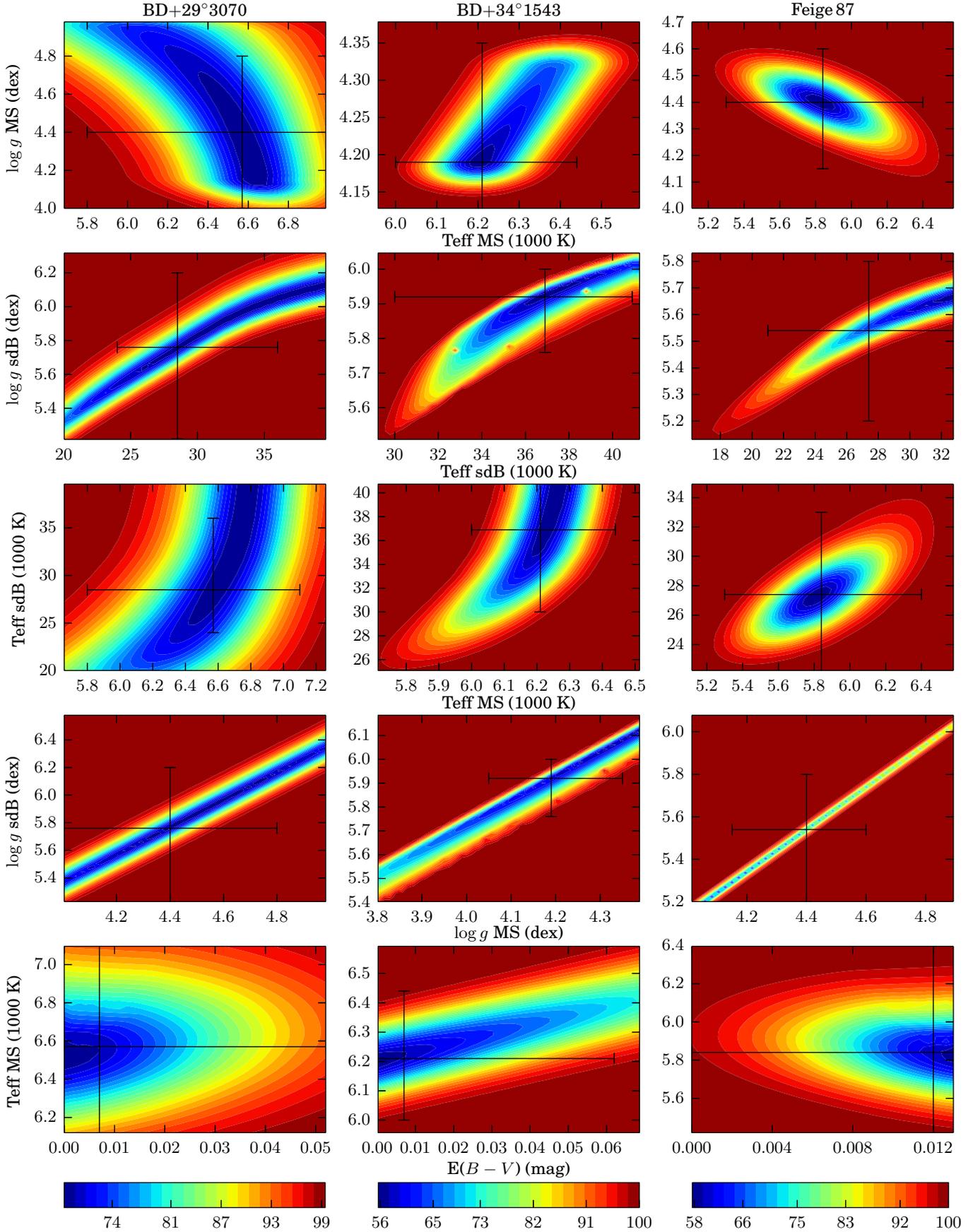
Fig. 4. Confidence intervals of the SED fits of BD+29°3070, BD+34°1543 and Feige 87. The different colors show the cumulative density probability connected to the χ^2 statistics given by Eq. (3). The best fitting values and there errors are plotted in black.
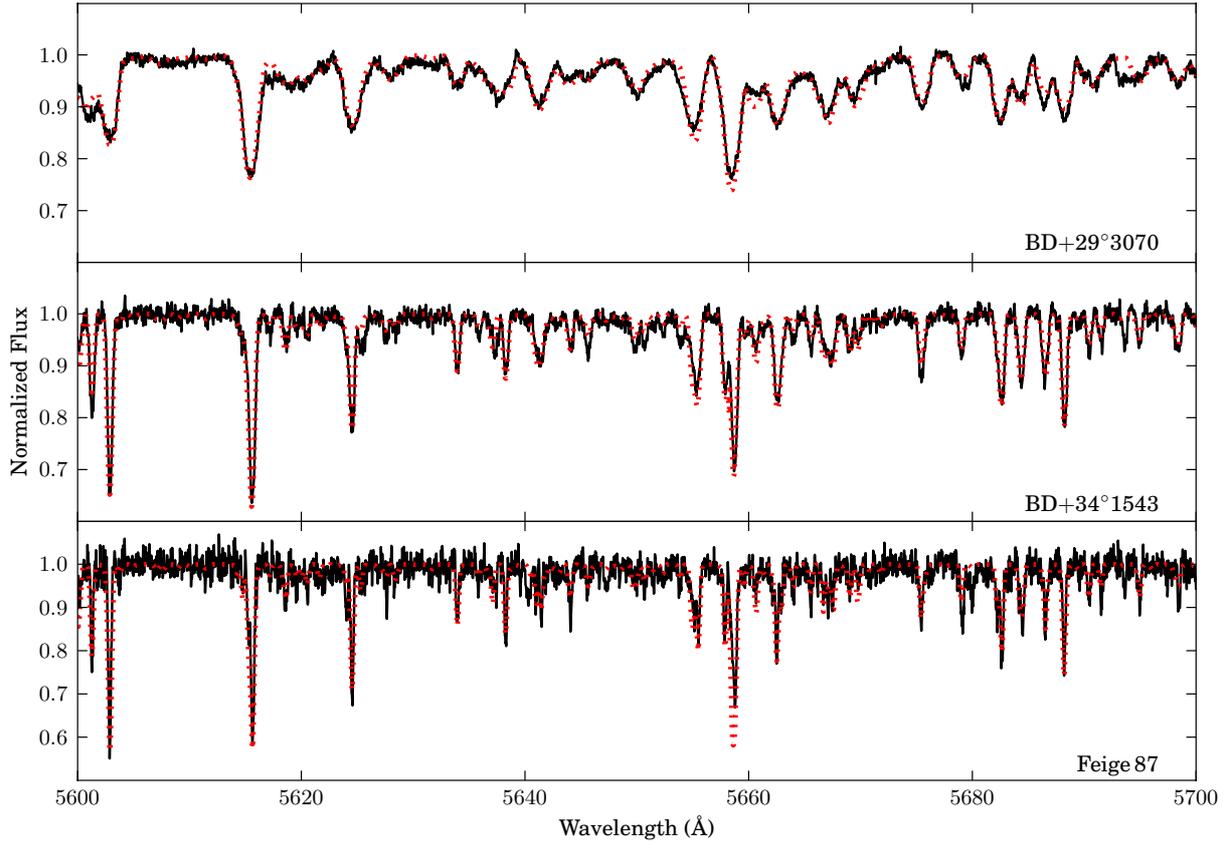
Fig. 5. Disentangled HERMES spectra of the MS components obtained by subtracting the sdB continuum and averaging all spectra (black full line), together with Kurucz model atmospheres based on the atmospheric parameters determined from the iron lines (red dotted line). *Top*: BD+29°3070, *center*: BD+34°1543, *bottom*: Feige 87.

polynomial to the spectrum. Then the continuum contribution of the sdB component is subtracted following:

$$F_{\text{tot}}(\lambda) = F_{\text{MS}}(\lambda)\frac{C(\lambda)}{1 + F_{\text{rat}}(\lambda)} + F_{\text{sdB}}(\lambda)\frac{C(\lambda) \cdot F_{\text{rat}}(\lambda)}{1 + F_{\text{rat}}(\lambda)}. \quad (4)$$

Where F_{tot} is the total flux in the HERMES spectrum, F_{MS} and F_{sdB} are the normalized fluxes of the MS and sdB components, C is the continuum of the HERMES spectrum, and F_{rat} is the ratio of the sdB flux to the MS flux. As only the regions where the sdB component does not have significant lines are used, $F_{\text{sdB}}(\lambda) = 1$ for every λ. The normalized MS spectrum is then given by:

$$F_{\text{MS}}(\lambda) = \left(F_{\text{tot}}(\lambda) - \frac{C(\lambda) \cdot F_{\text{rat}}(\lambda)}{1 + F_{\text{rat}}(\lambda)}\right) \Big/ \left(\frac{C(\lambda)}{1 + F_{\text{rat}}(\lambda)}\right). \quad (5)$$

The obtained MS spectra are shifted to zero velocity, and averaged weighted by their S/N. An example region of the final extracted spectra for both systems is plotted in Fig. 5.

This way of disentangling the spectra is dependent on the atmospheric parameters of both components, which means that the disentangling process needs to be repeated when a new set of atmospheric parameters for the MS component is derived from the iron lines. This is done until convergence, which happened for all systems after two iterations. The parameters of the sdB component cannot be derived from the resulting spectra, but tests were performed to check their influence. As it turns out, changing the T_{eff} or $\log g$ of the sdB component within the errors determined in the SED fitting process, does not have a significant effect on the parameters of the MS component derived from the iron lines.

4.2. Atmospheric parameters and abundances

The Versatile Wavelength Analysis[3] (VWA) tool developed by Bruntt et al. (2002) is used to determine the effective temperature, surface gravity, microturbulent velocity and abundances of the MS components. VWA generates synthetic spectra using the SYNTH software of Valenti & Piskunov (1996). Atomic line data is taken from the VALD database (Kupka et al. 1999), but the $\log(gf)$ values are adjusted so that every line measured by Wallace et al. (1998) reproduces the atmospheric abundances by Grevesse et al. (2007). The atmosphere models are interpolated from MARCS model atmospheres (Gustafsson et al. 2008) using the solar composition of Grevesse et al. (2007). The VWA package fits abundances in a semi-automatic way. It first selects the least blended lines in the spectra, and determines the abundances of these lines by calculating synthetic spectra for each line while iteratively changing the input abundance until the equivalent widths of the observed and synthetic spectrum match. The main advantage of VWA is that the synthetic spectrum includes the contribution of neighboring lines, thus making it possible to analyze stars with a high rotational velocity. A detailed description of the VWA software can be found in Bruntt et al. (2004, 2008); Bruntt (2009); Bruntt et al. (2010a,b).

Before the spectra are analyzed, they are carefully normalized with the RAINBOW tool of the VWA package. Then the spectra are compared to synthetic spectra, and projected rotational velocities of 52 ± 5 km s^{-1}, 17 ± 4 km s^{-1} and 8 ± 3 km s^{-1} are found for the G-star components of respectively BD+29°3070,

---

[3] https://sites.google.com/site/vikingpowersoftware/

Table 8. Abundances ([El/H]) for the MS components of BD+29°3070, BD+34°1543 and Feige 87 obtained from the disentangled HERMES spectra.

| | BD+29°3070 | | BD+34°1543 | | Feige 87 | |
Ion	[El/H]	N^a	[El/H]	N^a	[El/H]	N^a
Al I	0.26 ± 0.1	2				
Si I	0.24 ± 0.19	8	-0.12 ± 0.08	11	-0.38 ± 0.13	9
Si II	0.25	1	-0.21 ± 0.06	2		
Ca I	0.03	1	-0.14 ± 0.04	7	-0.27 ± 0.06	7
Sc II			-0.09	1	-0.70 ± 0.13	3
Ti I			-0.05 ± 0.06	3	0.09 ± 0.25	2
Ti II			-0.07 ± 0.12	2	-0.77	1
Cr I			-0.27 ± 0.13	4	-0.51 ± 0.04	2
Cr II	0.08	1	-0.25	1		
Mn I			-0.07	1	-0.82	1
Mg I					-0.12	1
Fe I	0.04 ± 0.16	34	-0.26 ± 0.07	50	-0.49 ± 0.17	51
Fe II	0.1 ± 0.18	3	-0.26 ± 0.12	6	-0.60 ± 0.4	3
Ni I	0.08 ± 0.16	6	-0.34 ± 0.10	11	-0.40 ± 0.25	12
Na I					-0.44	1

Notes. [a] Number of lines used per ion, the stated error is the rms error computed if two or more lines are available.

BD+34°1543 and Feige 87. Especially BD+29°3070 has a high rotational velocity, resulting in severe line blending, which makes it difficult to derive the atmospheric parameters. These parameters are determined using only the iron lines. The effective temperature is determined by requiring the abundance of the Fe I lines to be independent of the excitation potential. The surface gravity is derived by requiring the same abundance for Fe I and Fe II lines, and checked by fitting synthetic spectra to several calcium and magnesium lines that are sensitive to changes in $\log g$ (Gray 2005). Furthermore the independence of abundance on equivalent width gives the microturbulence velocity. When the atmospheric parameters are determined the final abundances of all measured lines are calculated, and the overall metallicity is obtained by averaging all abundances over the measured elements weighted by the number of lines found for each element.

The disentangled spectrum of BD+29°3070 has the highest S/N of the three systems ($S/N \sim 130$), making it possible to derive robust parameters regardless of the high rotational blending. In total, 401 suitable lines were selected after comparing the data with a synthetic spectrum. In the abundance determination process 56 lines (of which 34 Fe I and 3 Fe II lines) were used and had an equivalent width between 10 and 90 mÅ. The three Fe II lines have too large scatter to constrain the surface gravity and are ignored for this purpose. To obtain an estimate of the surface gravity three calcium lines (Ca λ 6122, Ca λ 6162, Ca λ 6439) and the magnesium triplet (Mg-1b λ 5172) are fitted with synthetic spectra. This resulted in a surface gravity of $\log g = 4.3 \pm 0.5$ dex. Using the surface gravity determined from the Ca and Mg lines, the atmospheric parameters determined based on the Fe I lines are: $T_{\rm eff} = 6100 \pm 200$ K and $v_{\rm micro} = 1.50 \pm 0.35$ km s^{-1}. The overall metallicity calculated using all 56 lines is [M/H] = 0.09 ± 0.21. The abundances of all lines are given in Table 8.

Having a lower rotational velocity and a still a high $S/N \sim 90$, more useful lines (578) were found in BD+34°1543. After the fitting process 99 lines (including 50 Fe I and 6 Fe II lines) were fitted and had an equivalent width between 10 and 90 mÅ. In this case the scatter on the abundances of the Fe II lines was low, we used it together with the Fe I lines to constrain the surface gravity, resulting in $\log g = 4.2 \pm 0.3$ dex. This value

is supported by fitting synthetic spectra to the same Ca and Mg lines as for BD+29°3070. Based on the Fe I lines an effective temperature of $T_{\rm eff} = 6150 \pm 150$ K and a microturbulence of $v_{\rm micro} = 1.45 \pm 0.25$ km s^{-1} were found. The averaged metallicity is found to be slightly sub solar at [M/H] = -0.24 ± 0.12. The abundances of all elements are shown in Table 8.

Feige 87 has the lowest rotational velocity, but this advantage is partly countered by the low S/N of the disentangled spectrum ($S/N \sim 35$). From the 428 selected lines 93 were used (including 51 Fe I lines and 3 Fe II lines). The scatter of the Fe II lines is high compared to the previous system, thus they are not very reliable in constraining the surface gravity. Based on fitting synthetic spectra to Ca and Mg lines, and on the ionization balance between Fe I and Fe II, we find a surface gravity of $\log g = 4.5 \pm 0.6$ dex. Based on the Fe I lines, the effective temperature is constrained to $T_{\rm eff} = 6175 \pm 150$ K and the microturbulence results in $v_{\rm micro} = 1.15 \pm 0.25$ km s^{-1}. The average metallicity based on 96 lines in total is clearly sub solar at [M/H] = -0.48 ± 0.26. The abundances of all elements are shown in Table 8.

4.3. Spectral fitting

F and G type MS companions of sdB stars can be easily resolved in the optical as they have similar brightnesses and distinct spectra. This allows one to disentangle such composite spectra from a single observation without knowing the radii or fluxes of the components. Such a binary decomposition was implemented in the XTGRID (Németh et al. 2012) spectral fitting algorithm and was used to estimate the atmospheric parameters of the components in 29 composite spectra binaries. XTGRID employs the NLTE model atmosphere code TLUSTY (Hubeny & Lanz 1995) for the subdwarf component and interpolated MILES (Cenarro et al. 2007) template spectra for the MS companion. The binary spectrum is fitted with a linear combination of the two components. This method is independent from the SED and VWA analysis and was applied for low-resolution flux calibrated spectra obtained with the B&C spectrograph, therefore it can be used to check the consistency of the different approaches.

Without preliminary assumptions on the spectral types XTGRID confirmed the results of the SED and VWA analysis on BD+29°3070 and BD+34°1543 within error bars, but predicted a lower surface gravity of the components in Feige 87. Then, with the help of the radial velocity measurements, we could constrain the surface gravities of the companions which helped achieving a better consistency of the decomposition in all three cases. Our results are listed in Table 9 and the disentangled binary spectra are plotted in Fig. 6. We note that the lower contribution of the MS star in Feige 87 raises the uncertainties of our parameter determination.

5. Gravitational redshift

If the difference between the surface gravity of both components in a binary system is substantial, this can give rise to a frequency shift in the emitted radiation. This effect is caused by a difference in gravitational redshift for the two stars. From general relativity one can derive that the gravitational redshift as function of the mass and surface gravity of the star (Einstein 1916):

$$z_g = \frac{1}{c^2} \sqrt{GMg}. \tag{6}$$

Where z_g is the gravitational redshift, c the speed of light, G the gravitational constant, M the mass, and g the surface gravity.
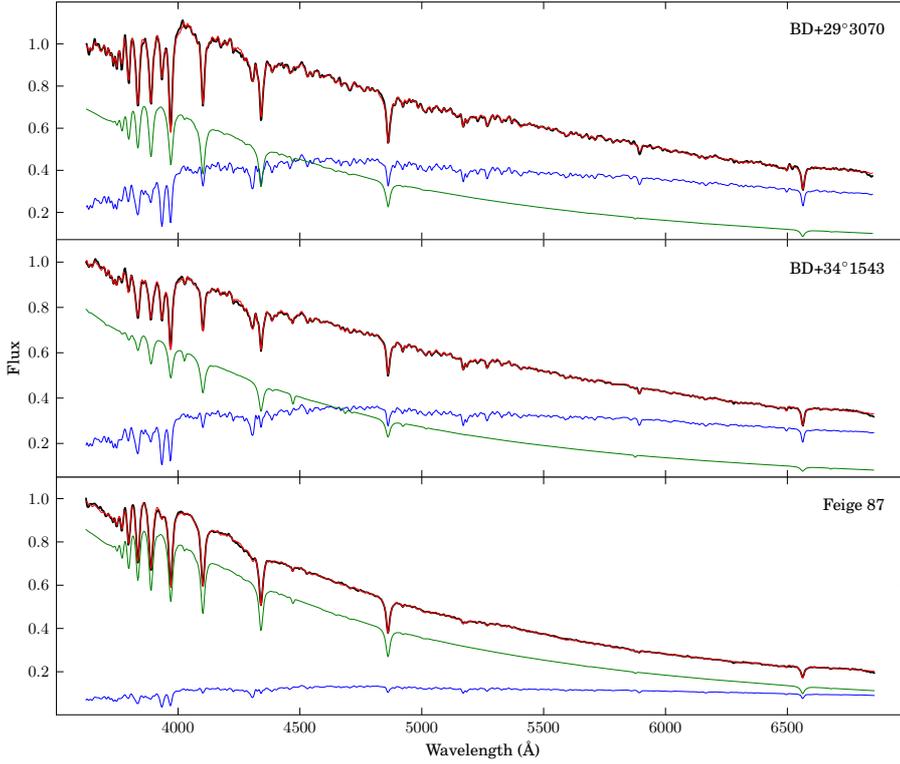
Fig. 6. Flux calibrated B&C spectra observed with the Bok telescope (black line) of BD+29°3070, BD+34°1543 and Feige 87 together with the best fitting binary atmosphere models from the XTGRID code (red line). The decomposition of the model in the MS and sdB component is plotted in respectively blue and green.

Table 9. Atmospheric parameters obtained from the flux calibrated spectra of BD+29°3070, BD+34°1543 and Feige 87.

Parameter	BD+29°3070	BD+34°1543	Feige 87
$E(B-V)$ (mag)	0.013	0.002	0.000
Flux ratio[a]	1.353	1.337	2.252
	MS component		
$T_{\rm eff}$ (K)	6026 ± 300	5715 ± 300	5675 ± 250
$\log g$ (dex)	4.26 ± 0.30	4.11 ± 0.30	4.23 ± 0.35
[Fe/H]	0.08 ± 0.25	-0.37 ± 0.25	-0.39 ± 0.25
	sdB component		
$T_{\rm eff}$ (K)	25380 ± 990	36640 ± 810	27270 ± 500
$\log g$ (dex)	5.54 ± 0.18	6.13 ± 0.16	5.47 ± 0.15
He[b]	$-2.63^{+0.48}_{-1.26}$	-1.49 ± 0.13	$-2.56^{+0.22}_{-0.50}$
C[b]	$-3.27>$	$-4.64>$	$-3.77>$
N[b]	$-2.79>$	$-3.28>$	$-3.69>$
O[b]	$-1.93>$	$-3.72>$	$-2.89>$

Notes. [a] Flux ratio $F_{\rm sdB}/F_{\rm MS}$ in wavelength range 6720−6800 Å. [b] Abundance given as $\log(nX/nH)$.

This z_g will effectively change the apparent systemic velocity for the star. In a binary system the difference in surface gravity for both components will be visible as a difference in systemic velocity between the components. As z_g is proportional to the square root of the surface gravity, this effect is only substantial when there is a large difference in $\log g$ between the components, as is the case for compact subdwarfs and MS stars.

The difference in systemic velocity between the MS and sdB component measured in the radial velocity curves can be used to estimate the surface gravity of the sdB component (see also Paper I). Using a canonical value of 0.47 $M_\odot$ for the sdB component and the mass ratio, the mass of the MS component can be calculated. Together with the surface gravity of the MS component derived from the SED fit and spectral analysis, the z_g of

the MS component can be calculated. The z_g of the sdB component can then be derived by combining $z_{g,\rm MS}$ with the measured difference in systemic velocity, and can be converted to an estimated surface gravity for the sdB component. A caveat here is that the wavelength of the He I λ 5875 multiplet is only known with a presision of ~0.01 Å, corresponding to a systematic radial velocity uncertainty of up to ~0.5 km s^{-1}. The measured shift in systemic velocity could be partly due to this uncertainty, but since the observations are consistent with the predicted gravitational redshift we believe this to be the main contributor.

For BD+29°3070, the system velocity of the sdB component is weakly constrained and does not yield a very constrained surface gravity for the sdB component. However, the system velocities of the other two systems are better constrained. The measured differences in system velocity for the three systems are:

$$\gamma_{\rm sdB} - \gamma_{\rm MS} = \begin{cases} 0.73 \pm 1.46 \text{ km s}^{-1} & (\text{BD} + 29°3070) \\ 1.01 \pm 0.52 \text{ km s}^{-1} & (\text{BD} + 34°1543) \\ 1.34 \pm 0.51 \text{ km s}^{-1} & (\text{Feige } 87). \end{cases} \quad (7)$$

Using the averaged values for the surface gravity of the MS components as given in Table 10, the estimated surface gravities of the sdB components of these systems are:

$$\log(g)_{\rm sdB} = \begin{cases} 5.41^{+0.30}_{-0.62} \text{ dex} & (\text{BD} + 29°3070) \\ 5.45^{+0.14}_{-0.34} \text{ dex} & (\text{BD} + 34°1543) \\ 5.73^{+0.12}_{-0.37} \text{ dex} & (\text{Feige } 87). \end{cases} \quad (8)$$

The asymmetrical error on the surface gravity is calculated using a Monte-Carlo simulation taking into account the error on the difference in system velocity and the errors on the parameters of the MS component. The resulting surface gravities correspond with the results from the other methods presented in this paper.

Table 10. Fundamental properties for both the main-sequence (MS) and subdwarf (sdB) component of BD+29°3070, BD+34°1543 and Feige 87.

Parameter	BD+29°3070 MS	BD+29°3070 sdB	BD+34°1543 MS	BD+34°1543 sdB	Feige 87 MS	Feige 87 sdB
P (d)	1283 ± 63		972 ± 2		936 ± 2	
T_0	2453877 ± 41		2451519 ± 11		2453259 ± 21	
e	0.15 ± 0.01		0.16 ± 0.01		0.11 ± 0.01	
ω	1.60 ± 0.22		1.58 ± 0.07		2.92 ± 0.15	
γ (km s^{-1})	−57.58 ± 0.36		32.10 ± 0.06		32.98 ± 0.08	
q	0.39 ± 0.01		0.57 ± 0.01		0.55 ± 0.01	
a ($R_\odot$)	586 ± 12		447 ± 4		442 ± 3	
i (°)	81 ± 5		43 ± 1		75 ± 2	
$E(B-V)$	0.010 ± 0.030		0.005 ± 0.030		0.006 ± 0.030	
d (pc)	238 ± 25		207 ± 30		383 ± 40	
[Fe/H]	0.05 ± 0.16		−0.26 ± 0.08		−0.50 ± 0.18	
K (km s^{-1})	6.53 ± 0.30	16.6 ± 0.6	5.91 ± 0.07	10.31 ± 0.15	8.19 ± 0.11	15.01 ± 0.21
M ($M_\odot$)	1.19 ± 0.09	0.47 ± 0.05	0.82 ± 0.07	0.47 ± 0.05	0.86 ± 0.07	0.47 ± 0.05
$\log g$ (cgs)	4.32 ± 0.50	5.56 ± 0.44	4.18 ± 0.40	5.84 ± 0.35	4.36 ± 0.42	5.54 ± 0.34
R ($R_\odot$)	1.25 ± 0.97	0.19 ± 0.10	1.21 ± 0.48	0.14 ± 0.06	1.02 ± 0.50	0.19 ± 0.07
$T_{\rm eff}$ (K)	6180 ± 420	25 900 ± 3000	6100 ± 300	36 600 ± 3000	5980 ± 325	27 300 ± 2700
L ($L_\odot$)	2.06 ± 0.25	14.3 ± 3.0	1.83 ± 0.25	30.13 ± 4.0	1.19 ± 0.20	18.04 ± 3.0
V_0 (mag)	10.91 ± 0.10	11.47 ± 0.15	10.72 ± 0.10	11.11 ± 0.15	12.54 ± 0.10	12.36 ± 0.15
M_V (mag)	4.02 ± 0.10	4.58 ± 0.15	4.14 ± 0.10	4.54 ± 0.15	4.62 ± 0.10	4.44 ± 0.15

Notes. The sdB mass is the canonical value.

6. Absolute parameters

Combining the results of the SED fit, the spectral analysis, grav-itational redshift and the orbital parameters derived from the ra-dial velocity curves, the absolute dimensions of BD+29°3070, BD+34°1543 and Feige 87 can be determined. With the as-sumed canonical sdB mass of $M_{\rm sdB} = 0.47\ M_\odot$, the inclina-tion of the systems can be derived from the reduced mass de-termined in Sect. 2.2. This inclination can be used to calculate the semi-major axis of the systems. The atmospheric parameters ($T_{\rm eff}$, $\log g$) determined with the four different methods (SED fit-ting, derived from the iron lines, spectral fitting and from the gravitational-redshift) correspond well within their errors. The final values for these parameters are the averages of the three methods weighted by their errors. The radii of the components is calculated from the mass and surface gravity. The system ve-locity is set to the system velocity of the MS component as the sdB component is subjected to significant gravitational redshift as discussed in Sect. 5.

The luminosity of both components can be calculated using $L = 4\pi\sigma R^2 T^4$. The apparent V magnitudes are obtained directly from the SED fitting procedure, while the absolute magnitude can be obtained by integrating the best fit model SEDs over the Johnson V band, and scaling the resulting flux to a distance of 10 pc. The distance to the system is then calculated from $\log d = (m_V - M_V + 5)/5$. For BD+34°1543 the distance obtained in this way corresponds within errors with the distance obtained from the Hipparcos parallax 236 ± 80 pc. The absolute dimensions of all three systems are summarized in Table 10.

The proper motions of BD+29°3070, BD+34°1543 and Feige 87 as measured by van Leeuwen (2007) are:

$$(\mu_\alpha, \mu_\delta) = (-6.29, 23.92) \pm (1.00, 1.55)\ \text{mas yr}^{-1} \qquad (9)$$
$$(\mu_\alpha, \mu_\delta) = (34.46, -61.08) \pm (2.28, 1.42)\ \text{mas yr}^{-1} \qquad (10)$$
$$(\mu_\alpha, \mu_\delta) = (14.12, -65.51) \pm (1.49, 1.82)\ \text{mas yr}^{-1}. \qquad (11)$$

Using the method of Johnson & Soderblom (1987), these num-bers together with the measured value of γ, can be used to

compute the galactic space velocity vector with respect to the lo-cal standard of rest from Dehnen & Binney (1998). Resulting in

$$(U, V, W)_{\rm LSR} = (-43.0, -27.1, -6.8) \pm (3.1, 1.5, 1.8)\ \text{km s}^{-1} \quad (12)$$
$$(U, V, W)_{\rm LSR} = (-13.0, -69.9, 28.1) \pm (0.9, 4.8, 2.3)\ \text{km s}^{-1} \quad (13)$$
$$(U, V, W)_{\rm LSR} = (95.1, -32.5, 94.1) \pm (13.9, 8.5, 9.0)\ \text{km s}^{-1} \quad (14)$$

for respectively BD+29°3070, BD+34°1543 and Feige 87. U is defined as positive towards the galactic center. Following the se-lection criteria of Reddy et al. (2006), all systems are bound to the galaxy, and belong to the thin or thick disk population.

7. Eccentric orbits

The three systems presented here are part of a sample consisting of six sdB + MS binaries, of which four systems have been anal-ysed up till now. The first system PG 1104+243 was described in Paper I, and is the only one from our sample with a circu-lar orbit ($P = 753$ d, $e < 0.002$). The two remaining systems (Balloon 82800003 and BD−7°5977) have longer periods that have not yet been covered completely at all phases, but prelim-inary results were presented in Vos et al. (2013) demonstrat-ing that both systems are significantly eccentric. Furthermore (Barlow et al. 2013) analysed PG 1449+653 ($P = 909$ d, $e = 0.11$) and PG 1701+359 ($P = 734$ d, circular), and (Deca et al. 2012) published results of PG 1018+243 which has a possible eccentric orbit ($P = 759$ d, $e \approx 0.2$). At the time of this pub-lication, there are nine long period sdB + MS systems know of which six have a significant eccentric orbit, one might have an eccentric orbit and two have a circular orbit.

Current theory predicts only circular orbits for these long period sdB binaries formed through the stable RLOF channel. During the red giant phase of the sdB progenitor the tidal forces between the sdB progenitor and its companion should circular-ize the orbit very efficiently (Zahn 1977), and the further evolu-tion provides very few possibilities to re-introduce eccentricity to the orbit. Deca et al. (2012) proposed the hierarchial triple

merger scenario of Clausen & Wade (2011) for the possibly eccentric sdB + K system PG 1018-047, where the K-type companion would not have been involved in the evolution of the sdB component. However, such a scenario seems too unlikely to be observed frequently.

Another possible explanation for these eccentric systems would be that tidal circularization during the RGB and the RLOF phase is not as efficient as currently assumed. In highly eccentric systems the mass transfer through RLOF and mass loss due to stellar winds will not be constant over the orbit. Bonačić Marinović et al. (2008) studied this effect in binary systems with an AGB star, and found that enhanced mass loss from the AGB star at orbital phases closer to periastron can work efficiently against the tidal circularization of the orbit. Further theoretical studies could investigate if this eccentricity enhancement mechanism can work in in the progenitors of sdB + MS binaries as well.

A last interesting observation of this small sample is that the two circular systems and PG 1018+243 with a possible circular orbit, have the shortest orbital periods. Although the sample is too small to state strong conclusions, this might support the above claim that the circularization process is not as efficient as expected and does not fully circularize the longer period systems.

8. Conclusions

Using both literature photometry and observed spectra, detailed astrophysical parameters of BD+29°3070, BD+34°1543 and Feige 87 have been established. The long time-base spectroscopic observations made it possible to determine accurate periods, and to solve the orbit of both the MS and sdB component in all three systems. The atmospheric parameters were determined with three different techniques: based on the SED, using iron lines in the disentangled MS spectra, and from low-resolution flux calibrated spectra. Furthermore, the measured gravitational-redshift could be used to derive the surface gravity of the sdB components. The results obtained with these different methods agree within their errors.

The sdB components of all three systems are consistent with a canonical post-core-helium-flash model with a mass around 0.47 $M_\odot$. However, the orbits of these systems are clearly eccentric, as opposed to what the current theory predicts. The periods found here correspond with the updated version of the BPS studies of Chen et al. (2013), although a significant degree of atmospheric RLOF must be included in order to reach the ~1300 d period of BD+29°3070. Furthermore, Chen et al. (2013) finds a metallicity – orbital period relation, where the orbital period will decrease with decreasing metallicity. The observed periods of BD+29°3070, BD+34°1543 and Feige 87 (1283 d, 972 d, 936 d) for metallicities (solar, about half solar, about 1/3rd solar) follow the metallicity relation, but significantly exceed the predictions of Chen et al. (2013). The same conclusion can be reached for PG 1104+243 (P = 753 d, ~1/3rd solar, Paper I). We assume that the metallicity measured for the companion is comparable to the initial Z for the system, which ignores any contamination during RLOF, and can therefore be considered as an upper limit to the initial Z. All four systems call for the inclusion of atmospheric RLOF, also at lower metallicities. While the sample is too limited yet to make conclusions with respect to the period distribution, the long periods found in this paper indicates that an additional mechanism such as atmospheric RLOF is required for all the systems, not just those with periods >1100 d, as suggested by Chen et al. (2013).

BD+29°3070, BD+34°1543 and Feige 87 are part of an ongoing long-term observing program of sdB + MS binaries with HERMES at *Mercator*. Currently most of the systems accessible with the 1.2 m *Mercator* + HERMES telescope-spectrograph combination have been analysed, but orbital solutions of more systems are needed in order to test the predicted orbital distributions. Our results call for the study of eccentricity pumping mechanisms (e.g. Bonačić Marinović et al. 2008) also in the framework of sdB binaries.

References

Allard, F., Wesemael, F., Fontaine, G., Bergeron, P., & Lamontagne, R. 1994, AJ, 107, 1565
Barlow, B. N., Wade, R. A., Liss, S. E., Østensen, R. H., & Van Winckel, H. 2012, ApJ, 758, 58
Barlow, B. N., Liss, S. E., Wade, R. A., & Green, E. M. 2013, ApJ, 771, 23
Bergeron, P., Fontaine, G., Lacombe, P., et al. 1984, AJ, 89, 374
Bonačić Marinović, A. A., Glebbeek, E., & Pols, O. R. 2008, A&A, 480, 797
Brassard, P., Fontaine, G., Billères, M., et al. 2001, ApJ, 563, 1013
Brown, T. M., Ferguson, H. C., Davidsen, A. F., & Dorman, B. 1997, ApJ, 482, 685
Bruntt, H. 2009, A&A, 506, 235
Bruntt, H., Catala, C., Garrido, R., et al. 2002, A&A, 389, 345
Bruntt, H., Bikmaev, I. F., Catala, C., et al. 2004, A&A, 425, 683
Bruntt, H., De Cat, P., & Aerts, C. 2008, A&A, 478, 487
Bruntt, H., Bedding, T. R., Quirion, P.-O., et al. 2010a, MNRAS, 405, 1907
Bruntt, H., Deleuil, M., Fridlund, M., et al. 2010b, A&A, 519, A51
Cenarro, A. J., Peletier, R. F., Sánchez-Blázquez, P., et al. 2007, MNRAS, 374, 664
Chen, X., Han, Z., Deca, J., & Podsiadlowski, P. 2013, MNRAS, 434, 186
Clausen, D., & Wade, R. A. 2011, ApJ, 733, L42
Copperwheat, C. M., Morales-Rueda, L., Marsh, T. R., Maxted, P. F. L., & Heber, U. 2011, MNRAS, 415, 1381
Cutri, R. M., Skrutskie, M. F., van Dyk, S., et al. 2003, VizieR Online Data Catalog, II/246
D'Cruz, N. L., Dorman, B., Rood, R. T., & O'Connell, R. W. 1996, ApJ, 466, 359
Deca, J., Marsh, T. R., Østensen, R. H., et al. 2012, MNRAS, 421, 2798
Degroote, P., Acke, B., Samadi, R., et al. 2011, A&A, 536, A82
Dehnen, W., & Binney, J. J. 1998, MNRAS, 298, 387
Einstein, A. 1916, Relativity: the special and general theory (Methuen & Co Publishing Ltd)
Fitzpatrick, E. L. 2004, in Astrophysics of Dust, eds. A. N. Witt, G. C. Clayton, & B. T. Draine, ASP Conf. Ser., 309, 33
Geier, S. 2013, in EPJ Web Conf., 43, 4001
Geier, S., Hirsch, H., Tillich, A., et al. 2011, A&A, 530, A28
Gray, D. F. 2005, The Observation and Analysis of Stellar Photospheres (CUP)
Green, R. F., Schmidt, M., & Liebert, J. 1986, ApJS, 61, 305
Green, E. M., Liebert, J., & Saffer, R. A. 2001, in 12th European Workshop on White Dwarfs, eds. J. L. Provencal, H. L. Shipman, J. MacDonald, & S. Goodchild , ASP Conf. Ser., 226, 192

Greggio, L., & Renzini, A. 1990, ApJ, 364, 35

Grevesse, N., Asplund, M., & Sauval, A. J. 2007, Space Sci. Rev., 130, 105

Gustafsson, B., Edvardsson, B., Eriksson, K., et al. 2008, A&A, 486, 951

Han, Z., Tout, C. A., & Eggleton, P. P. 2000, MNRAS, 319, 215

Han, Z., Podsiadlowski, P., Maxted, P. F. L., Marsh, T. R., & Ivanova, N. 2002, MNRAS, 336, 449

Han, Z., Podsiadlowski, P., Maxted, P. F. L., & Marsh, T. R. 2003, MNRAS, 341, 669

Heber, U. 1998, in Ultraviolet Astrophysics Beyond the IUE Final Archive, eds. W. Wamsteker, R. Gonzalez Riestra, & B. Harris, ESA SP, 413, 195

Heber, U. 2009, ARA&A, 47, 211

Heber, U., Reid, I. N., & Werner, K. 2000, A&A, 363, 198

Heber, U., Moehler, S., Napiwotzki, R., Thejll, P., & Green, E. M. 2002, A&A, 383, 938

Hubeny, I., & Lanz, T. 1995, ApJ, 439, 875

Johnson, D. R. H., & Soderblom, D. R. 1987, AJ, 93, 864

Kharchenko, N. V. 2001, Kinematika i Fizika Nebesnykh Tel, 17, 409

Koen, C., Orosz, J. A., & Wade, R. A. 1998, MNRAS, 300, 695

Kupka, F., Piskunov, N., Ryabchikova, T. A., Stempels, H. C., & Weiss, W. W. 1999, A&AS, 138, 119

Kurucz, R. L. 1979, ApJS, 40, 1

Lucy, L. B., & Sweeney, M. A. 1971, AJ, 76, 544

Maxted, P. F. L., Moran, C. K. J., Marsh, T. R., & Gatti, A. A. 2000, MNRAS, 311, 877

Maxted, P. f. L., Heber, U., Marsh, T. R., & North, R. C. 2001, MNRAS, 326, 1391

Mengel, J. G., Norris, J., & Gross, P. G. 1976, ApJ, 204, 488

Mermilliod, J.-C., Mermilliod, M., & Hauck, B. 1997, A&AS, 124, 349

Morales-Rueda, L., Maxted, P. F. L., Marsh, T. R., North, R. C., & Heber, U. 2003, MNRAS, 338, 752

Napiwotzki, R., Karl, C. A., Lisker, T., et al. 2004, Ap&SS, 291, 321

Nelemans, G. 2010, Ap&SS, 329, 25

Nelemans, G., Verbunt, F., Yungelson, L. R., & Portegies Zwart, S. F. 2000, A&A, 360, 1011

Nelemans, G., Yungelson, L. R., Portegies Zwart, S. F., & Verbunt, F. 2001, A&A, 365, 491

Németh, P., Kawka, A., & Vennes, S. 2012, MNRAS, 427, 2180

Østensen, R. H. 2006, Balt. Astron., 15, 85

Østensen, R. H., & Van Winckel, H. 2011, in Evolution of Compact Binaries, eds. L. Schmidtobreick, M. R. Schreiber, & C. Tappert, ASP Conf. Ser., 447, 171

Østensen, R. H., & Van Winckel, H. 2012, in Fifth Meeting on Hot Subdwarf Stars and Related Objects, eds. D. Kilkenny, C. S. Jeffery, & C. Koen, ASP Conf. Ser., 452, 163

Paczynski, B. 1976, in Structure and Evolution of Close Binary Systems, eds. P. Eggleton, S. Mitton, & J. Whelan, IAU Symp., 73, 75

Pfeiffer, M. J., Frank, C., Baumueller, D., Fuhrmann, K., & Gehren, T. 1998, A&AS, 130, 381

Raskin, G., van Winckel, H., Hensberge, H., et al. 2011, A&A, 526, A69

Reddy, B. E., Lambert, D. L., & Allende Prieto, C. 2006, MNRAS, 367, 1329

Richmond, M. W. 2007, PASP, 119, 1083

Saffer, R. A., Bergeron, P., Koester, D., & Liebert, J. 1994, ApJ, 432, 351

Schlegel, D. J., Finkbeiner, D. P., & Davis, M. 1998, ApJ, 500, 525

Sweigart, A. V. 1997, ApJ, 474, L23

Valenti, J. A., & Piskunov, N. 1996, A&AS, 118, 595

van Leeuwen, F. 2007, A&A, 474, 653

Vos, J., Østensen, R. H., Degroote, P., et al. 2012, A&A, 548, A6

Vos, J., Østensen, R. H., & Van Winckel, H. 2013, in 6th Meeting on Hot Subdwarf Stars and Related Objects, eds. E. Green, & G. Fontaine, PASPC, in press

Wallace, L., Hinkle, K., & Livingston, W. 1998, An atlas of the spectrum of the solar photosphere from 13 500 to 28 000 cm^{-1} (3570 to 7405 Å) (Tuscon: National Optical Astronomy Observatories)

Webbink, R. F. 1984, ApJ, 277, 355

Werner, K., Deetjen, J. L., Dreizler, S., et al. 2003, in Stellar Atmosphere Modeling, eds. I. Hubeny, D. Mihalas, & K. Werner, ASP Conf. Ser., 288, 31

Zahn, J.-P. 1977, A&A, 57, 383

Table 1. Observing dates (mid-time of exposure) and exposure times of the spectra of BD+29°3070, BD+34°1543 and Feige 87.

BD+29°3070		BD+34°1543		Feige 87	
BJD −2 450 000	Exp. s	BJD −2 450 000	Exp. s	BJD −2 450 000	Exp. s
5029.4643	1800	5166.5252	700	5028.4488	1800
5040.4568	1800	5218.5730	600	5028.4703	1800
5055.4675	1200	5238.5505	900	5028.4917	1800
5060.3980	1210	5238.5664	900	5251.7145	890
5321.6137	1500	5238.5775	900	5251.7247	390
5351.4739	1500	5240.5316	1800	5341.5722	1603
5425.4024	1600	5475.6918	900	5351.4184	2700
5619.7185	1500	5502.7281	900	5371.4175	2700
5638.6611	1700	5507.6955	900	5566.7810	2700
5648.6732	1500	5553.5767	900	5616.6402	2100
5658.6816	1600	5614.5668	900	5622.7074	720
5670.5225	1500	5621.5560	800	5622.7317	2000
5678.5495	1940	5658.3476	594	5656.6032	911
5686.5327	1800	5807.7326	600	5658.5870	1210
5701.5513	1750	5844.6708	900	5660.6107	704
5718.4729	2000	5861.7131	900	5663.5411	1200
5745.4261	1950	5887.6807	900	5666.5345	1800
5761.5685	1800	5932.5869	900	5937.7967	1800
5772.5841	1950	5942.6039	1200	5964.6900	3400
5778.4452	1700	5949.5190	900	5965.5843	2400
5795.3894	1500	5954.4967	1000	5968.6517	1800
5808.3721	1500	5965.4262	1100	5990.7225	1800
5829.3696	1500	5968.6346	900	6017.6145	1500
5999.7619	900	5978.5722	1050	6042.4773	1800
6027.6990	1500	6007.5012	820	6060.4147	1800
6049.5559	1500	6043.4301	900	6064.5674	1800
6082.5484	1150	6058.3969	1500	6066.4652	1800
6135.4325	800	6066.3756	1800	6068.4574	1800
6135.4423	800	6068.3894	1250	6082.4504	1800
6139.4292	1400	6069.3668	900	6138.4374	1800
6145.4352	1000			6141.4016	1800
				6196.3415	1800
				6301.7679	1800

Table 2. Radial velocities of both components of BD+29°3070.

	MS component		sdB component	
BJD −2 450 000	RV km s^{-1}	Error km s^{-1}	RV km s^{-1}	Error km s^{-1}
5029.4643	−52.88	0.26	−68.81	0.66
5040.4568	−52.93	0.29	−67.11	0.54
5057.9327	−53.60	0.31	−67.54	0.63
5321.6137	−62.78	0.24	−42.40	0.63
5351.4739	−63.33	0.28	−41.13	0.70
5425.4024	−64.21	0.32	−38.11	0.92
5619.7185	−61.96	0.26	−47.31	0.40
5638.6611	−61.48	0.26	−46.01	0.60
5648.6732	−61.46	0.28	−49.33	0.42
5658.6816	−61.23	0.28	−49.87	0.46
5670.5225	−60.54	0.31	−49.68	0.65
5678.5495	−60.54	0.29	−49.87	0.57
5686.5327	−60.53	0.28	−50.48	1.51
5701.5513	−60.16	0.26	−50.08	0.45
5718.4729	−59.57	0.31	−51.23	0.62
5745.4260	−58.64	0.27	−53.05	0.56
5761.5685	−57.96	0.27	−54.34	0.47
5772.5840	−57.41	0.42	−55.12	1.16
5778.4452	−57.97	0.27	−56.52	0.53
5795.3894	−57.04	0.26	−56.18	0.52
5808.3721	−57.29	0.26	−57.48	0.81
5829.3696	−56.31	0.27	−60.02	0.49
5999.7619	−53.06	0.30	−68.54	0.60
6027.6990	−52.27	0.24	−69.76	0.54
6049.5559	−52.56	0.28	−70.69	0.59
6082.5484	−51.93	0.26	−71.97	0.52
6136.7680	−51.29	0.30	−71.20	0.97
6145.4352	−51.17	0.27	−73.82	0.56

Table 3. Radial velocities of both components of BD+34°1543.

	MS component		sdB component	
BJD −2 450 000	RV km s^{-1}	Error km s^{-1}	RV km s^{-1}	Error km s^{-1}
1576.5166[a]	29.23	0.25	38.66	1.02
5166.5252	37.78	0.28	22.99	1.06
5218.5730	38.22	0.16	23.70	0.64
5239.0565	37.89	0.18	22.93	0.85
5475.6918	28.84	0.15	40.31	0.72
5505.2118	27.43	0.18	39.93	0.59
5553.5767	26.53	0.14	42.56	0.41
5614.5668	26.06	0.18	43.16	0.86
5621.5560	26.32	0.15	43.37	0.55
5658.3476	26.49	0.18	42.43	1.07
5807.7326	29.81	0.16	37.27	0.66
5844.6708	30.83	0.16	36.26	0.54
5861.7131	31.03	0.14	35.21	0.48
5887.6807	32.11	0.16	33.09	0.44
5932.5869	33.17	0.14	30.80	0.47
5942.6039	33.67	0.14	31.00	0.43
5952.0079	33.85	0.14	31.00	0.47
5967.0304	34.00	0.16	30.38	0.45
5978.5721	34.43	0.17	28.29	0.69
6007.5012	35.16	0.14	26.71	0.47
6043.4301	36.11	0.15	25.59	0.61
6058.3969	36.20	0.22	25.36	1.45
6068.0440	36.10	0.18	24.30	0.77

Notes. [a] FOCES spectrum.

Table 4. Radial velocities of both components of Feige 87.

BJD −2 450 000	MS component RV km s^{-1}	MS component Error km s^{-1}	sdB component RV km s^{-1}	sdB component Error km s^{-1}
5028.4488	28.02	0.12	42.74	0.48
5341.5722	31.03	0.13	39.20	0.71
5351.4184	31.74	0.31	37.43	0.93
5371.4175	32.33	0.25	35.43	0.47
5566.7810	40.20	0.35	22.72	0.59
5616.6402	40.42	0.31	22.35	0.69
5622.7074	39.77	0.35	20.36	0.47
5656.6032	39.63	0.36	21.10	0.86
5663.5411	39.78	0.38	20.40	0.49
5937.7967	29.72	0.16	41.10	0.58
5964.6900	28.30	0.32	42.98	0.50
5990.7225	26.68	0.17	46.81	0.75
6017.6145	24.14	0.81	46.12	0.95
6042.4773	24.42	0.37	49.18	0.80
6060.4147	24.30	0.37	51.28	1.11
6066.4651	24.04	0.25	50.75	0.63
6082.4504	23.80	0.28	50.80	0.62
6196.3415	26.92	0.29	45.67	0.72
6301.7679	32.12	0.30	36.19	0.48

Table 6. Photometry of BD+29°3070, BD+34°1543 and Feige 87 collected from the literature.

Band	Wavelength Å	Width Å	Magnitude mag	Error mag
BD+29°3070				
Johnson U^a	3640	550	10.030	0.020
Johnson B^a	4450	940	10.600	0.020
Johnson V^a	5500	880	10.420	0.020
Johnson B^b	4450	940	10.590	0.013
Johnson V^b	5500	880	10.416	0.013
Johnson V^c	5500	880	10.376	0.052
Cousins I^c	7880	1490	10.026	0.053
Geneva U^a	3460	170	10.264	0.010
Geneva B^a	4250	283	9.638	0.010
Geneva V^a	5500	298	10.359	0.010
Geneva $B1^a$	4020	171	10.523	0.011
Geneva $B2^a$	4480	164	11.103	0.011
Geneva $V1^a$	5400	202	11.075	0.011
Geneva G^a	5810	206	11.476	0.011
2MASS J^d	12410	1500	9.773	0.020
2MASS H^d	16500	2400	9.621	0.023
2MASS K_s^d	21910	2500	9.546	0.022
BD+34°1543				
Johnson B^b	4450	940	10.293	0.014
Johnson V^b	5500	880	10.145	0.013
Johnson V^c	5500	880	10.156	0.048
Cousins I^c	7880	1490	9.758	0.077
Geneva U^a	3460	170	9.759	0.008
Geneva B^a	4250	283	9.362	0.009
Geneva V^a	5500	298	10.140	0.007
Geneva $B1^a$	4020	171	10.215	0.010
Geneva $B2^a$	4480	164	10.865	0.010
Geneva $V1^a$	5400	202	10.854	0.010
Geneva G^a	5810	206	11.260	0.010
2MASS J^d	12410	1500	9.485	0.023
2MASS H^d	16500	2400	9.326	0.033
2MASS K_s^d	21910	2500	9.207	0.018
Feige 87				
Johnson B^e	4450	940	11.598	0.050
Johnson V^e	5500	880	11.693	0.050
Cousins R^e	6470	1515	11.671	0.050
Cousins I^e	7880	1490	11.623	0.050
Stromgren U^f	3500	300	11.800	0.045
Stromgren V^f	4110	190	11.747	0.045
Stromgren B^f	4670	180	11.698	0.045
Stromgren Y^f	5470	230	11.730	0.090
2MASS J^d	12410	1500	11.484	0.022
2MASS H^d	16500	2400	11.359	0.026
2MASS K_s^d	21910	2500	11.312	0.022

References. $^{(a)}$ Mermilliod et al. (1997); $^{(b)}$ Kharchenko (2001); $^{(c)}$ Richmond (2007); $^{(d)}$ Cutri et al. (2003); $^{(e)}$ Allard et al. (1994); $^{(f)}$ Bergeron et al. (1984).